# Investigation and Suppression of Current Zero Crossing Phenomenon for a Semicontrolled Open-Winding PMSG System

Heng Nian, *Senior Member, IEEE*, and Yijie Zhou

***Abstract*—The semicontrolled open-winding PMSG system has been widely investigated due to its simplified topology and easy control implementation. Nevertheless, compared with the conventional controllable converter structure, the current zero crossing phenomenon will last a longer time in the semicontrolled configuration, which is determined by the phase displacement between voltage and current. Since a long current zero crossing duration will lead to voltage pulse disturbance, serious electromagnetic interference, and output power fluctuation, it is necessary to reduce the zero crossing duration to improve the open-winding PMSG performance. This paper gives a detailed analysis on the zero crossing phenomenon of the semicontrolled open-winding PMSG system in the 3-D space vector modulation perspective. Meanwhile, a third harmonic injection method is suggested to reduce the zero crossing duration. It is also demonstrated that the torque and power pulsation are effectively improved, while the zero-sequence current amplitude does not increase. A proportional resonant controller is used to regulate the desired zero-sequence current. The proposed method is validated in a 1-kW semicontrolled open-winding PMSG experimental system with $i_d = 0$ control method.**

***Index Terms*—Open-winding PMSG system, semicontrolled configuration, third harmonic injection, three-dimensional (3-D) space vector modulation.**

## I. Introduction

CONVERTER topologies and the corresponding pulse width modulation (PWM) schemes have been extensively studied for the open-winding configuration in the past few decades [1]–[11]. By employing different converters combination, the open-winding configuration can provide more degree of freedom for the control, implement multilevel or polygonal modulation performance, and improve the operation capability of motors [5]–[8]. Since the permanent magnet synchronous generator (PMSG) takes the advantages of high power density, flexible magnet topologies, and excellent operation performance, the combination of open-winding configuration and PMSG system has been regarded as a promising topology in the medium-voltage high-power applications. However, a large amount of switch devices are essential in the open-winding PMSG configuration, which will not only increase the system expense but also make it difficult and complex for modulation implementation [9]–[11]. Therefore, it is important to simplify the configuration of the open-winding PMSG system for its further development.

In the existed literature, the diode has been applied to replace the switching device in both doubly fed induction generator and PMSG system [12]–[15]. Although the diode converter can reduce the system expense and control complexity, the current is seriously distorted and the torque will be deteriorated in this case. Meanwhile, a semicontrolled converter has been proposed to simplify the PMSG-based wind energy conversion system [16], which can take a compromise between the fully controlled voltage source converter (VSC) and the uncontrolled diode converter.

In the recent studies, the semicontrolled converter has been adopted in the open-winding PMSG system with common dc bus and isolated dc bus [17]–[19]. Due to the simpler configuration, the common dc bus topology will have a priority in the practical application. Based on the inherent characteristic of the semicontrolled converter, two indispensable requirements should be satisfied in order to achieve a zero-sequence current totally suppression performance: 1) accurate zero-sequence current suppression regulator, and 2) unity power factor control method [18], [19]. In [18], an active common mode current regulator was proposed to minimize the zero-sequence current. Meanwhile, a proportional resonant (PR) controller was presented in [19] to suppress the zero-sequence current. Both of these two literatures have demonstrated that the zero-sequence current could not be perfectly suppressed with nonzero power factor angle (PFA). For the semicontrolled topology, it is an inevitable problem that the current can just be regulated to have the same direction with voltage [18].

However, in most PMSG control methods, PFA is not zero, i.e., *d*-axis current zero, maximum torque current ratio, field weakening, etc. With the method proposed in [18] and [19], the zero-sequence current cannot be totally suppressed and it will lead to the current zero crossing phenomenon. Different from the transient current zero crossing distortion in the conventional controllable converter structure [20], [21], the current zero crossing phenomenon lasts a longer time which is determined by the phase displacement between voltage and current. As a result, the current zero crossing phenomenon will lead to voltage pulse disturbance, serious electromagnetic interference (EMI), and output power fluctuation. Until now, few literatures focus on the operation performance improvement caused by nonzero PFA in

Manuscript received September 1, 2015; revised December 6, 2015; accepted January 21, 2016. Date of publication January 29, 2016; date of current version September 16, 2016. Recommended for publication by Associate Editor J. R. Rodriguez.

The authors are with the College of Electrical Engineering, Zhejiang University, Hangzhou 310027, China (e-mail: nianheng@zju.edu.cn; zhouyijie@zju.edu.c).

Color versions of one or more of the figures in this paper are available online at http://ieeexplore.ieee.org.

Digital Object Identifier 10.1109/TPEL.2016.2523252

the common dc supplied semicontrolled open-winding PMSG system.

In order to improve the open-winding PMSG performance in the semicontrolled configuration, this paper aims to analyze the nature of zero crossing phenomenon with a 3-D space vector modulation perspective. With an appropriate third harmonic current injection, the current zero crossing phenomenon can be eliminated. Meanwhile, the voltage pulse disturbance, EMI, and output power fluctuation will be efficiently improved.

This paper is organized with seven sections. In Section II, the mathematical model of the PMSG and semicontrolled converter are presented. Section III gives the current zero crossing phenomenon analysis, and a third harmonic injection method is proposed in this section. Section IV presents a discussion on the comparison of operation performance. The control diagram for the semicontrolled system is shown in Section V to implement the current regulation. In Section VI, the simulation results are presented. A 1-kW experimental setup is developed to validate the proposed control method and modulation technique shown in Section VII. Finally, Section VIII presents the conclusion.

## II. Mathematical Modeling of Semicontrolled Open-Winding PMSG System

### A. Open-Winding PMSG Mathematical Model

The common dc bus supplied semicontrolled open-winding PMSG system is shown in Fig. 1. The power obtained by the PMSG is transferred by the coordinating operation of both converters. With the zero-sequence equation taken into consideration, the PMSG mathematical model in synchronous rotating *dq0* frame can be expressed as [22], [23],

$$\begin{bmatrix} u_d \\ u_q \\ u_0 \end{bmatrix} = \begin{bmatrix} -L_d p - R & \omega L_q & 0 \\ -\omega L_d & -L_q p - R & 0 \\ 0 & 0 & -L_0 p - R \end{bmatrix} \begin{bmatrix} i_d \\ i_q \\ i_0 \end{bmatrix} + \begin{bmatrix} 0 \\ \omega \psi_{1r} \\ -3\omega \psi_{3r} \sin(3\theta_r) \end{bmatrix} \tag{1}$$

where $u_{dq0}$ and $i_{dq0}$ are the *dq0* voltage and current components, respectively, $L_0$ is the zero-sequence inductance, $L_d$ and $L_q$ are the *d*-axis and *q*-axis inductances, $R$ is the phase winding resistance, $\omega$ is the electrical angular speed, $\theta_r$ is the electrical position, $\psi_{1r}$ and $\psi_{3r}$ are the fundamental and third component of the rotor flux, and $p$ is the differential operator.

Meanwhile, the electromagnetic torque $T_e$ and active power output $P_e$ can be derived as

$$\begin{aligned} T_e &= \frac{3n_p}{2\omega}(e_d i_d + e_q i_q + 2e_0 i_0) \\ &= \frac{3}{2} n_p \left[ L_q i_q i_d + (\psi_{1r} - L_d i_d) i_q - 6\psi_{3r} \sin(3\theta_r) i_0 \right] \\ P_e &= \frac{\omega T_e}{n_p}. \end{aligned} \tag{2}$$

According to (1) and (2), it can be seen that all *dq0*-axis component make contribution to the operation performance of open-winding PMSG.

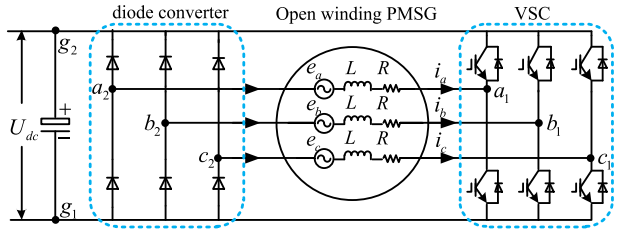


Fig. 1. Common dc bus supplied semicontrolled open-winding PMSG system.

TABLE I
Relationship Between the Current Direction and $u_{\alpha\beta 0-2}$ Modulated by Diode Bridge Converter

| Current Direction | | | | Vector | Value | | |
|---|---|---|---|---|---|---|---|
| subsector | $i_a$ | $i_b$ | $i_c$ | $u_{\alpha\beta 0-2}$ | $u_{\alpha-2}$ | $u_{\beta-2}$ | $u_{0-2}$ |
| 1 | P | N | N | (0 1 1) | $-2U_{\rm dc}/3$ | 0 | $2U_{\rm dc}/3$ |
| 2 | P | P | N | (0 0 1) | $-U_{\rm dc}/3$ | $-\sqrt{3}U_{\rm dc}/3$ | $U_{\rm dc}/3$ |
| 3 | N | P | N | (1 0 1) | $U_{\rm dc}/3$ | $-\sqrt{3}U_{\rm dc}/3$ | $2U_{\rm dc}/3$ |
| 4 | N | P | P | (1 0 0) | $2U_{\rm dc}/3$ | 0 | $U_{\rm dc}/3$ |
| 5 | N | N | P | (1 1 0) | $U_{\rm dc}/3$ | $\sqrt{3}U_{\rm dc}/3$ | $2U_{\rm dc}/3$ |
| 6 | P | N | P | (0 1 0) | $-U_{\rm dc}/3$ | $\sqrt{3}U_{\rm dc}/3$ | $U_{\rm dc}/3$ |

### B. Semicontrolled Converter Mathematical Model

Generally, the space vector diagram for fully controllable VSC is just determined by the switching state combination. Thus, a good modulation performance can be achieved as long as the voltage vector reference locates in the linear modulation region. However, since a diode converter is applied in the semicontrolled open-winding configuration, the hybrid space vector diagram is decided by not only the switching state of the controllable converter but also the current polarity flowing through the diode converter. As a result, the available modulation region is limited and alternates according to the three-phase current polarity.

For the open-winding PMSG system, the $\alpha\beta 0$ voltage component can be obtained by coordinate transformation as the *dq0* voltage reference is regulated. Meanwhile, the hybrid voltage space vector is determined by both converters, which can be written as,

$$u_{\alpha\beta 0} = u_{\alpha\beta 0-1} - u_{\alpha\beta 0-2} \tag{3}$$

where $u_{\alpha\beta 0}$ represents the hybrid voltage vector generated by the semicontrolled system; $u_{\alpha\beta 0-1}$ and $u_{\alpha\beta 0-2}$ are the voltage vectors generated by the VSC and diode converter, respectively.

Since the voltage output by the diode converter is determined by three-phase current direction, the instantaneous phase voltage of open-winding PMSG modulated by the diode converter can be expressed as

$$\begin{cases} u_{a2g1} = [1 - \mathrm{sgn}(i_a)]\, U_{\rm dc} \\ u_{b2g1} = [1 - \mathrm{sgn}(i_b)]\, U_{\rm dc} \\ u_{c2g1} = [1 - \mathrm{sgn}(i_c)]\, U_{\rm dc} \end{cases} \tag{4}$$

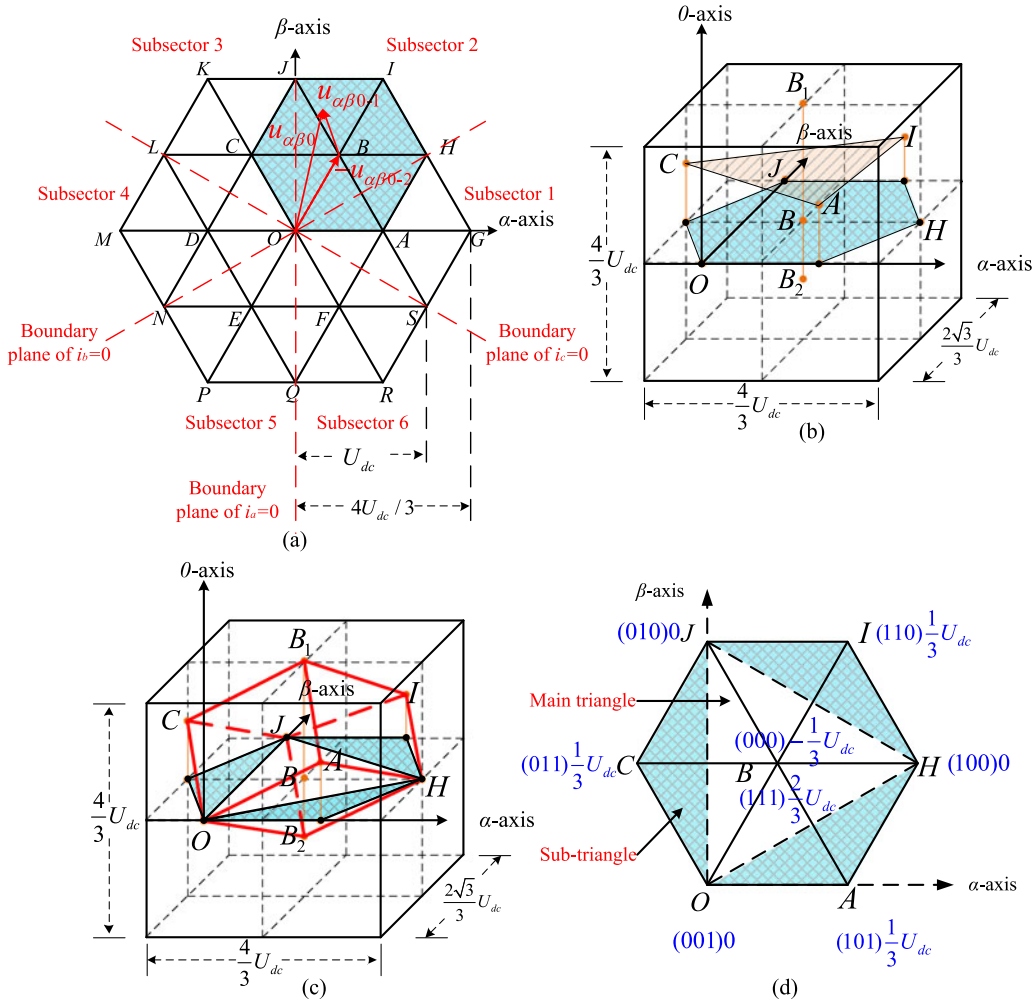


Fig. 2. Voltage space vector diagram for the semicontrolled system. (a) Space vector scheme of the semicontrolled open-winding PMSG system with its projection on $\alpha\beta$ plane. (b) Vertex geometrical location in 3-D coordinate. (c) Voltage space vector 3-D modulation range. (d) Projection of the 3-D modulation range in $\alpha\beta$ plane.

where $U_{\rm dc}$ represents the dc-link voltage, and the sign function can be expressed as

$$\mathrm{sgn}(i_j) = \begin{cases} 1, & \text{if}(i_j > 0), \\ 0, & \text{if}(i_j < 0), \end{cases} \quad j = a, b, c \tag{5}$$

$$T_{\mathrm{abc}\to\alpha\beta 0} = \frac{2}{3}\begin{bmatrix} 1 & -1/2 & -1/2 \\ 0 & \sqrt{3}/2 & -\sqrt{3}/2 \\ \frac{1}{2} & \frac{1}{2} & \frac{1}{2} \end{bmatrix}. \tag{6}$$

With the transformation matrix from *abc*-axis to $\alpha\beta 0$-axis shown as (6), $u_{\alpha\beta 0-2}$ can be calculated. With different combination of three-phase currents, the diode converter can generate different statues in $\alpha\beta 0$ component as shown in Table I, where P and N represent the current in positive and negative directions, respectively.

According to the analysis above, Fig. 2(a) shows the space vector scheme of the semicontrolled open-winding PMSG system with its projection on $\alpha\beta$ plane. Since the current boundary condition in *abc*-axis is $i_a = 0, i_b = 0,$ or $i_c = 0$, the boundary condition in $\alpha\beta 0$ coordinate frame can be written as

$$\begin{cases} i_\alpha + i_0 = 0 \rightarrow \text{boundary plane of } i_a = 0 \\ -\frac{i_\alpha}{2} + \frac{\sqrt{3}i_\beta}{2} + i_0 = 0 \rightarrow \text{boundary plane of } i_b = 0 \\ -\frac{i_\alpha}{2} - \frac{\sqrt{3}i_\beta}{2} + i_0 = 0 \rightarrow \text{boundary plane of } i_c = 0. \end{cases} \tag{7}$$

In the $\alpha\beta 0$ 3-D space, the current boundary condition contributes to three different boundary planes as expressed in (7). These three planes intersect the $\alpha\beta$ plane with three boundary lines which can be derived as $i_\alpha = 0$, $i_\alpha - \sqrt{3}i_\beta = 0$ or $i_\alpha + \sqrt{3}i_\beta = 0$, shown as dotted lines in Fig. 2(a). Therefore, the $\alpha\beta$ plane can be divided into six subsectors by the current boundary lines, named as Subsector 1–6. As the current vector locates in different subsector, the available voltage vector modulation range will change.

In order to analyze the available modulation range of each subsector, it is assumed that $i_a$ and $i_b$ is positive, while $i_c$ is negative. In this case, the current vector locates in Subsector 2 and $u_{\alpha\beta 0-2}$ can be expressed as (0 0 1). According to (3), the controllable VSC could modulate voltage vector around the vertex of $-u_{\alpha\beta 0-2}$ which is shown as the center point *B* in Fig. 2(a).

TABLE II
ZERO-SEQUENCE VOLTAGE GENERATED BY EACH SUBSECTOR

| Subsector | 1 | 2 | 3 |
|---|---|---|---|
| Subtriangles zero-sequence voltage | Negative | Positive | Negative |
| Subsector | 4 | 5 | 6 |
| Subtriangles zero-sequence voltage | Positive | Negative | Positive |

Therefore, the available modulation region is the hexagon *HIJCOA*. In the hexagon, six vertexes represent switching states of six active vectors by the VSC, while the center point $B(B_1$ and $B_2$ in 3-D coordinate) represents two zero vector switching states. All these eight states make contribution to zero-sequence voltage components. The vertex geometrical location in 3-D coordinate is shown in Fig. 2(b). The zero-sequence components of each vertex are listed as

1) $2U_{\rm dc}/3$, $B_1(1\ 1\ 1)$;
2) $U_{\rm dc}/3$, $I(1\ 1\ 0)$, $C(0\ 1\ 1)$, $A(1\ 0\ 1)$;
3) $0$, $J(0\ 1\ 0)$, $O(0\ 0\ 1)$, $H(1\ 0\ 0)$;
4) $-U_{\rm dc}/3$, $B_2(0\ 0\ 0)$.

The available modulation range in 3-D coordinate frame can be obtained by connecting all these eight vertexes as shown in Fig. 2(c). It can be found that the available modulation range is a cube. Each side of the cube is a rhombus and the same to others. Meanwhile, the cube intersects the $\alpha\beta$ plane by the triangle *JOH*. Fig. 2(d) shows the projection of the 3-D modulation range in the $\alpha\beta$ plane which makes up a hexagonal region. The hexagonal region can be divided into four parts, three subtriangles *HIJ*, *JCO*, *OAH* and a main triangle *JOH*. According to Fig. 2(c), it can be seen that only positive zero-sequence voltage can be modulated in the subtriangle area. However, the main triangle area can contribute to both positive and negative zero-sequence voltage by redistributing zero vector dwell times.

With the same method, the available modulation range can also be divided as three subtriangles and one main triangle as the current vector locates in different subsector. Similarly with Subsector 2, the main triangle of other subsectors can also contribute to positive or negative adjustable zero-sequence components, while the subtriangles can just contribute positive or negative zero-sequence component as shown in Table II. Due to the semicontrolled converter structure, the available voltage space vector diagram is unique. The voltage vector reference should be kept in the available modulation region to realize a desired voltage output. Otherwise, the current waveform will be distorted.

## III. SUPPRESSION STRATEGY OF ZERO-SEQUENCE CURRENT OF THE SEMICONTROLLED SYSTEM

In order to obtain a stable electromagnetic torque as well as output active power, the *dq*-axis current component should be controlled as a dc value with low fluctuation. Meanwhile, the zero-sequence component should be suppressed as much as possible. Since the space vector diagram of the semicontrolled PMSG system is different from the conventional converter, the current vector will be absolutely influenced by the limited voltage vector modulation. The current vector trajectory

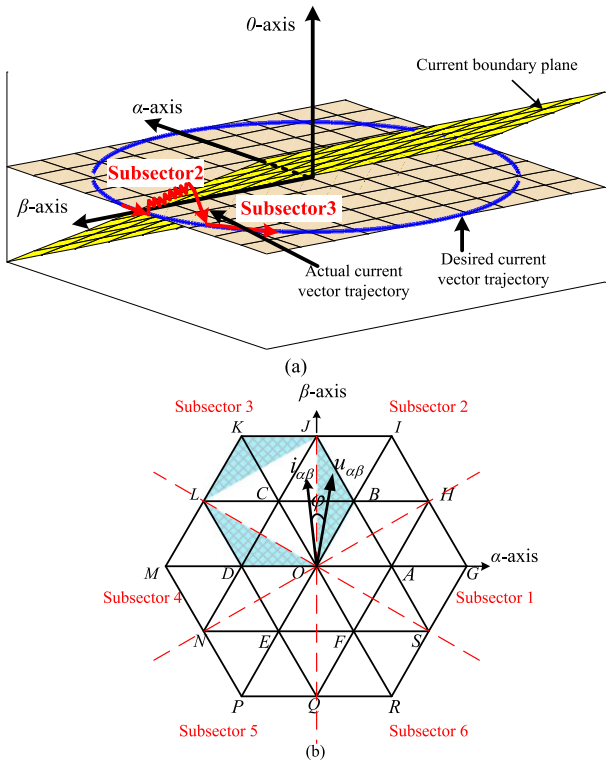


Fig. 3. Current vector trajectory with zero-sequence component suppression. (a) In $\alpha\beta 0$-axis 3-D space. (b) In $\alpha\beta$-axis 2-D plane.

analysis with nonzero PFA is presented here to give a detailed illustration.

### A. Current Vector Trajectory With Nonzero PFA

As mentioned in Section II, the modulation region is limited within a hexagonal area for the semicontrolled converter due to the current direction. Meanwhile, the zero-sequence voltage generated in the subtriangles area will be negative in subsector 1, 3, 5 and positive in subsector 2, 4, 6. According to 1), the negative zero-sequence voltage will result in a rapid increase in the zero-sequence current, while the positive zero-sequence voltage will lead to a rapid decrease in the zero-sequence current. As illustrated in (7), the current boundary planes are also determined by zero-sequence component. As a result, the increased or decreased zero-sequence current will make the current vector rotates through the current boundary plane. In this case, the available voltage vector modulation region will alternate to adjacent subsector. The dynamic trajectory will be analyzed in the following.

In the conventional zero-sequence current suppression method in [18], [19], the desired current vector trajectory is wished to be a circle located on the $\alpha\beta$ plane as shown in Fig. 3(a). With a nonzero PFA control method, the current vector will lead or lag the voltage vector with the PFA $\varphi$. In this example, assuming that the current vector leads the voltage vector, and if the current vector rotates to cross the current boundary plane from subsector 2 to subsector 3, the voltage vector still locates in subsector 2. The current boundary plane between subsectors 2 and 3 can be expressed as $i_\alpha + i_0 = 0$, which is shown in Fig. 3(a). The projection on plane is described as Fig. 3(b). In the

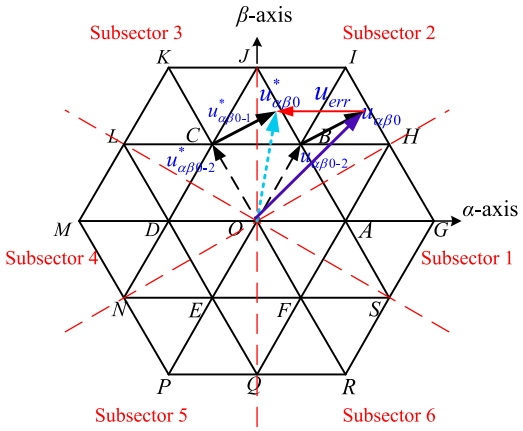


Fig. 4. Modulated voltage error as the current vector fluctuates around the current boundary plane.

subsector 3, subtriangle contributes to a negative zero-sequence voltage component. Since the negative voltage component will make the zero-sequence current increase, the current vector will reach the current boundary plane and go across the plane. Therefore, the current vector will go back to subsector 2. At this moment, the voltage vector location is in the main triangle of subsector 2. The zero-sequence current component will be controlled to be zero. Afterward, the current vector will go across the current boundary and get into subsector 3. As a result, the repetitive process lasts until the voltage vector rotates into subsector 3. This process appears at all six current boundary plane. It can be seen that the repetitive process duration is determined by the PFA.

### B. Influence Caused by Current Zero Crossing Phenomenon

In the conventional two-level VSC system, a current error will be enlarged during voltage vector sector switching. Since the sector switching duration takes a few control periods, the current error can be quickly suppressed in the VSC system [24]. However, according to the analysis above, the zero-sequence current suppression method leads to the current vector trajectory fluctuation on the current boundary plane. As a result, the sector switching duration takes a long time. Since the system voltage reference is modulated by the hybrid of both converters, it is important to get the instantaneous and accurate current direction to achieve an effective voltage modulation. However, as the current vector fluctuating on the current boundary plane and sampling frequency is bandwidth limited, there will be inevitable current sector judgement mistake in the sector switching duration. As shown in Fig. 4, due to the mistake in the subsector judgment, the real voltage vector generated by diode $u_{\alpha\beta 0-2}$ will be different by the reference $u^*_{\alpha\beta 0-2}$ calculated by DSP. As a result, the modulated voltage $u\alpha\beta 0$ will differ from the voltage reference $u^*_{\alpha\beta 0}$ with a voltage error $u_{\rm err}$. The voltage error will exist in the whole sector switching duration. Also, $u_{\rm err}$ will lead to the current fluctuation errors $\Delta i_d$ and $\Delta i_q$, which is the main reason for torque ripple and active power fluctuation.

### C. Third Harmonic Injection Method

According to the analysis above, in order to improve the operation performance, the current zero crossing duration should be reduced. Therefore, it is necessary to make the current vector go across the current boundary fast and unrepeated. In the case that the voltage vector rotates into the main triangle as the current vector goes from one subsector to another, the conditions can be satisfied. A zero-sequence current injection method is adopted here as shown in Fig. 5(a). The desired current vector trajectory contains a zero-sequence component, while its projection on the $\alpha\beta$ plane is still a circle. Since the zero-sequence component is injected, the moment that the current vector goes across the current boundary plane will lag for a duration compared with the suppression method. As a result, the equivalent current boundary plane on the plane is shown in Fig. 5(b). Consequently, the voltage vector will be always located in the main triangle and the current vector $\alpha\beta$ components fluctuation can be minimized.

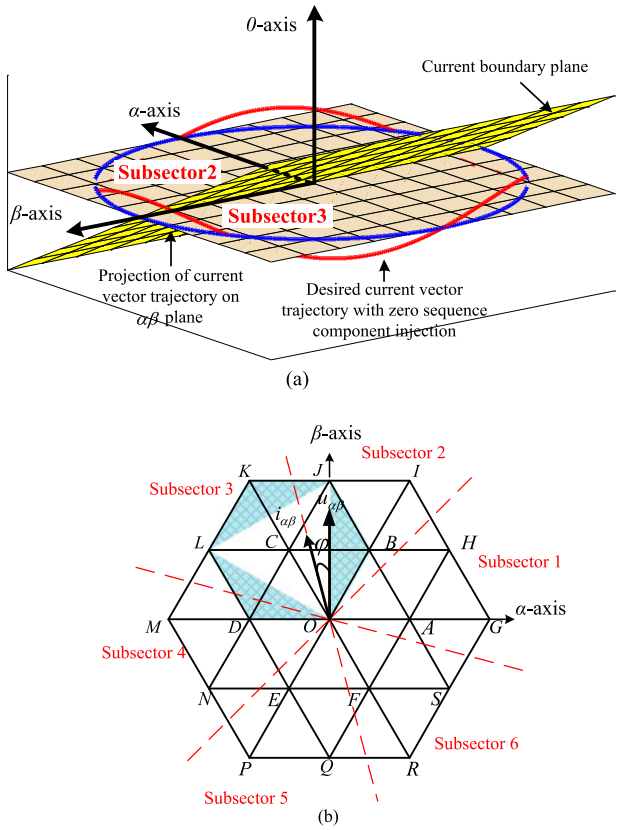


Fig. 5. Current vector trajectory without zero-sequence component injection. (a) In $\alpha\beta$0-axis 3-D space. (b) In $\alpha\beta$-axis 2-D plane.

### D. Third Harmonic Current Reference Calculation

According to the analysis mentioned above, a desired third harmonic can be injected to shift the current zero crossing point to synchronize the current and voltage. As shown in Fig. 6, with a desired third harmonic injection, the zero crossing point has been shifted with PFA $\varphi$.

According to the analysis mentioned above, a desired third harmonic can be injected to shift the current zero crossing point to synchronize the current and voltage. As shown in Fig. 6, with a desired third harmonic injection, the zero crossing point has been shifted with PFA $\varphi$.

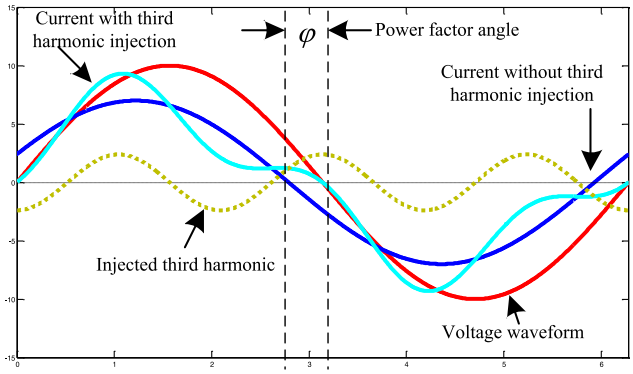


Fig. 6. Third harmonic current injection diagram.

Donating the original current component as $A_{\rm amp}\sin(\omega t)$, the injected third harmonic component as $B_{\rm amp}\sin(3\omega t+\theta)$, the reconstructed current with third harmonic injection can be derived as $A_{\rm amp}\sin(\omega t)+B_{\rm amp}\sin(3\omega t+\theta)$, where $A_{\rm amp}$ and $B_{\rm amp}$ represent the amplitude of fundamental and third component separately, $\omega t$ is the phase angle of stator current, $\theta$ is the initial phase angle of the third harmonic current.

Judging from the current expression, the original zero crossing point locates at $\omega t=p$. With the third harmonic injection, the zero crossing point will shift backward (or forward) with an angle. The modified zero crossing point locates at $\omega t=p$. As a result, it can be derived as

$$A_{\rm amp}\sin(\pi+\varphi)+B_{\rm amp}\sin[3(\pi+\varphi)+\theta]=0. \tag{8}$$

Equation (8) can be also expressed as

$$B_{\rm amp}=-\frac{A_{\rm amp}\sin(\pi+\varphi)}{\sin[3(\pi+\varphi)+\theta]}. \tag{9}$$

In order to reduce the amplitude of the third harmonic current to be minimized, the denominator in (9) should get the maximum value. As a result, it should be satisfied that $\sin[3(\pi+\varphi)+\theta]=1$. The phase angle and amplitude can be expressed as

$$\begin{aligned} B_{\rm amp} &= -A_{\rm amp}\sin(\varphi) \\ \theta &= -3\varphi-\frac{\pi}{2}. \end{aligned} \tag{10}$$

## IV. Operation Performance Discussion

Since a third harmonic injection method is adopted here to reduce the current zero crossing duration, the voltage pulse disturbance and EMI can be suppressed effectively.

With the proposed method, the zero-sequence current still exists. However, according to the current vector trajectory, it can be found that the subsector switching point is nearly the same for conventional zero-sequence suppression method and third harmonic injection method. Therefore, the amplitude of the injected third harmonic is approximately equal to the amplitude of zero-sequence component with conventional method. Meanwhile, the distortion for nonzero-sequence components has been effectively suppressed due to that less voltage error will be generated in the zero crossing duration. According to the qualitative analysis, the torque ripple appears to be reduced with the proposed method.

Although the third harmonic injection method can make some contributions to the performance of open-winding PMSG, the disadvantage can still be found.

First, the injected third harmonic current will lead to extra loss in the stator winding. According to (10), the injected third harmonic current has a relationship with the fundamental component. Since the harmonic current also contribute to the stator heating, the open-winding PMSG should be de-rated to avoid overheating. Combined with (10), the maximum fundamental current should be deduced as $1/\sqrt{1+\sin^2(\varphi)}$ of the rated current. Here, $1/\sqrt{1+\sin^2(\varphi)}$ can be named as derating ratio. The relationship between the PFA and derating ratio is shown in Fig. 7(a). It can be seen that the PMSG should be derated more as the PFA increase.

Second, according to (2), the electromagnetic power $P_e$ contains a six times frequency fluctuation, which is caused by the interaction of third harmonic back EMF and zero-sequence current. Since the third harmonic flux $\psi_{3r}$ is a small component, the extra six times power fluctuation is negligible. When the stator resistance is ignored, the power output by the PMSG is approximately equal to electromagnetic power. Third, similarly with the electromagnetic power, the electromagnetic torque will also contain a six times frequency fluctuation. With the combination of (2) and (10), the torque expression with third harmonic injection could be rewritten as

$$\begin{aligned} T_e &= \frac{3}{2}n_p\{L_q i_q i_d+(\psi_{1r}-L_d i_d)i_q-6\psi_{3r}\sqrt{(i_d)^2+(i_q)^2}\sin(\varphi) \\ &\quad\times\sin(3\theta_r)\sin[3\theta_r+3\arccos\left(\frac{i_d}{\sqrt{(i_d)^2+(i_q)^2}}\right)+\frac{\pi}{2}-3\varphi]\} \\ &= T_0+T_6\sin(6\theta_r+3\arccos\left(\frac{i_d}{\sqrt{(i_d)^2+(i_q)^2}}\right)+\frac{\pi}{2}-3\varphi) \end{aligned} \tag{11}$$

where $T_0$ is the dc component of electromagnetic torque and $T_6$ is the amplitude of six time frequency component.

Fig. 7(b) shows the relationship between $T_6$ and $T_0$. It can be seen that the torque fluctuation ratio depends on the third harmonic flux and PFA. Generally, the third harmonic flux is negligible and the power factor is higher than 0.8. As a result, the torque ripple caused by third harmonic is limited within a proper range.

## V. Semicotrolled Open-Winding PMSG System Control Diagram

The proposed system control scheme for the semicontrolled open-winding PMSG system is shown as Fig. 8, in which closed-loop regulators for all $dq0$-axis current are designed. With the $i_d=0$ control method, the $d$-axis current reference can be set as zero, while the $q$-axis current reference can be obtained for the power regulator. Meanwhile, the zero-sequence current regulator is designed for the third harmonic current injection. Since the

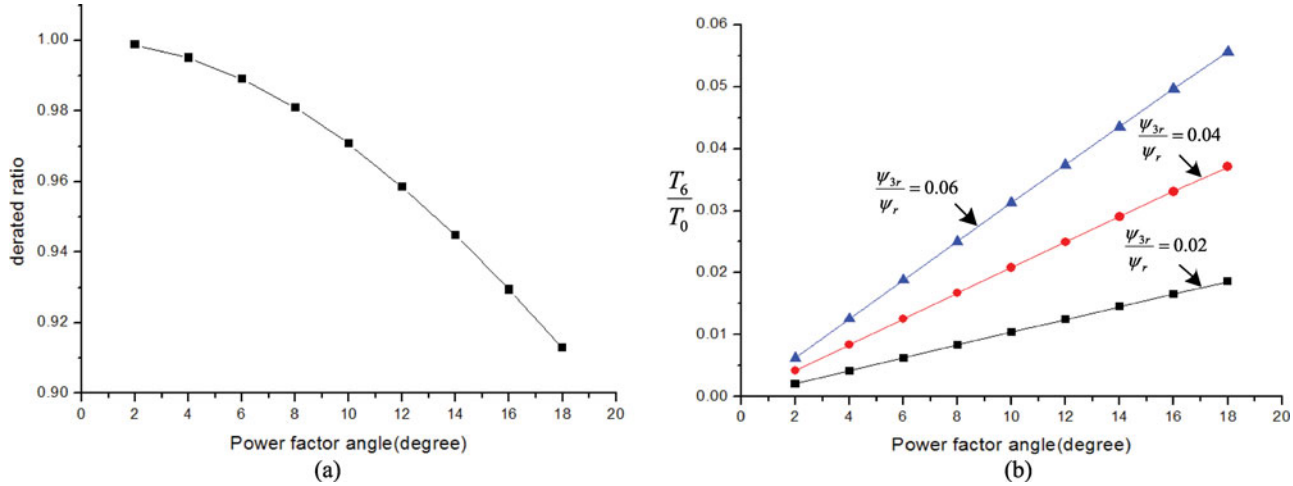


Fig. 7. Influences caused by PFA. (a) Relationship between PFA and derated ratio with third harmonic injection method. (b) Relationship between PFA and $T_6/T_0$ with third harmonic injection method.

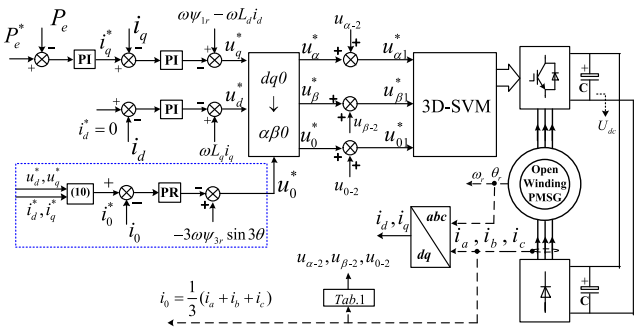


Fig. 8. Control scheme of open-winding PMSG system with zero-sequence current injection.

zero-sequence component is an ac component, a PR controller is selected to eliminate the tracking error [25].

According to the *dq*-axis current and voltage reference, the PFA and current amplitude can be easily calculated. Moreover, the amplitude and phase of the desired third harmonic current should be calculated as (10). The zero-sequence voltage reference can be derived as

$$\begin{aligned} \mu_0^* &= G_z(s)(i_0^* - i_0) - 3\omega\psi_{3r}\sin 3\theta_r \\ G_z(s) &= k_p + \frac{k_R\omega_c s}{s^2 + 2\omega_c s + \omega_0^2} \end{aligned} \tag{12}$$

where $k_p$ and $k_R$ represent proportional and resonant gains of the zero-sequence current suppression regulator, respectively. $\omega_c$ is the cut off frequency, while $\omega_0$ is the resonant frequency. In order to implement the zero-sequence current suppression, $\omega_0$ is selected as $3\omega$ and $\omega_c$ can be selected as 2–5 rad/s [26], [27]. The compensation term $-3\omega\psi_{3r}\sin 3\theta_r$ is added in the zero-sequence current suppression regulator based on the PMSG zero-sequence circuit model. In order to design the PR current regulator parameter, it should be satisfied to keep phase margin around 45° and gain margin around 4–6 dB, maintain constant gain at the resonant frequency with different resonant bandwidths [28]. Thus, the $k_p$ is set as 3, and $k_r$ is set as 70 in this paper.

TABLE III
OPEN-WINDING PMSG PARAMETERS FOR 2 MW SYSTEM

| Parameter | Value | Parameter | Value |
|---|---|---|---|
| Rated power $P_n$ | 2 MW | Rated speed $n$ | 18 r/min |
| Rated phase voltage $U_n$ | 415.5 V | Rated phase current $I_n$ | 1604.6 A |
| Rated frequency $f_n$ | 14.4 Hz | $d$-axis inductance $L_d$ | 0.254 mH |
| Stator $R_s$ | 0.00352 Ω | $q$-axis inductance $L_q$ | 0.254 mH |
| Pole pairs number $n_p$ number $n_p$ | 48 | 0-axis inductance $L_0$ | 0.043 mH |

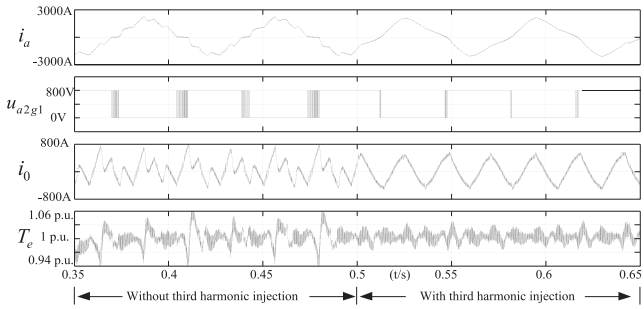


Fig. 9. Simulation results comparison for the semicontrolled system.

## VI. SIMULATION RESULTS

The simulation is performed using the MATLAB/Simulink. A 2-MW open-winding PMSG system with the semicontrolled configuration is built in the simulation. The simulation parameters are as follows: The dc bus is set as 600 V, switching frequency as 2 kHz. The parameter for 2-MW PMSG is listed in Table III.

The simulation results comparison between the third harmonic injection method and the conventional method is shown in Fig. 9. On the rated condition, it can be seen that the pulse disturbance in diode converter voltage is much more serious for the conventional method. With the third harmonic injection method, the pulse disturbance has been suppressed effectively. Meanwhile, torque ripple has been suppressed in ±2% with the third harmonic injection method, while the torque ripple is

TABLE IV
OPEN-WINDING PMSG PARAMETERS FOR 1 KW SYSTEM

| Parameter | Value | Parameter | Value |
|---|---|---|---|
| Rated power $P_n$ | 1 kW | Rated speed $n$ | 40 r/min |
| Rated phase voltage $U_n$ | 66.5 V | Rated phase current $I_n$ | 5 A |
| Rated frequency $f_n$ | 5.33 Hz | $d$-axis inductance $L_d$ | 77.56 mH |
| Stator $R_s$ | 1.1 Ω | $q$-axis inductance $L_q$ | 107.4 mH |
| Pole pairs number $n_p$ number $n_p$ | 8 | 0-axis inductance $L_0$ | 17 mH |

about ±6% with the conventional method. From the comparison of zero-sequence current, it can be seen that the amplitude of the zero-sequence current is almost the same and the zero-sequence current regulator works well. From the simulation results, it can be concluded that the third harmonic injection method contributes to the pulse disturbance and torque ripple suppression.

## VII. EXPERIMENTAL VALIDATION

The 1-kW semicontrolled open-winding PMSG experimental platform is established. The parameters for the open-winding PMSG are listed in Table IV. An adjustable dc power supply is used to establish the dc bus voltage. The VSC is built with SEMIKRON SKM75GB124DE IGBTs, while the diode converter is built with MDS100-16 Diodes. The VSC controller is implemented based on a TMS320F2812 development board, and SEMIKRON SKHI61 is used as the driver for IGBT. Sampling frequency and switching frequency are set as 8 kHz in the digit processing program. The experimental waveforms are acquired by a YOKOGAWA DL750 scope recorder. The dc bus is set as 120 V by the dc source. The block diagram of the experiment system is shown in Fig. 10(a) and the experimental apparatus is shown in Fig. 10(b).

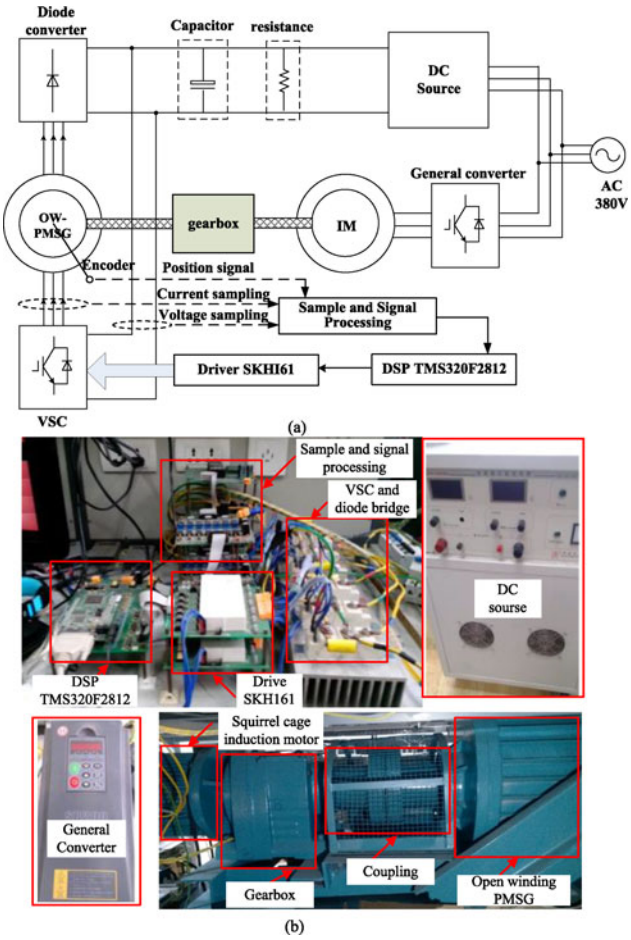


Fig. 10. Experimental setup.

Fig. 11 shows the experimental results comparison with two methods. Method 1 is the conventional zero-sequence current suppression method, while method 2 is the proposed zero-sequence current injection method. The speed of the open-winding PMSG is set as 40 r/min, while the electrical frequency is rated as 5.33 Hz. Fig. 11(a) and (b) shows the results of method 1 and 2 with 500-W power output reference. With method 1, the $q$-axis current fluctuates at 3.5 ± 0.2 A, while the $d$-axis current fluctuates from 0.1 to 0.2 A. The torque ripple varies at about 117∼124 N·m. Contrastively, the $q$-axis current fluctuates at 3.52 ± 0.1 A, while the $d$-axis current fluctuates from 0.1 to 0.1 A with method 2. The torque ripple is about 119–122 N·m. Since the PFA is small at this power output, the torque ripple keeps in a low value. It can be seen that the current vector trajectory on the $\alpha\beta$ plane circularized with method 2. Fig. 11(c) and (d) shows the results of method 1 and 2 with 1-kW power output reference. With method 1, the $q$-axis current fluctuates at 7.04 ± 0.5 A, while the $d$-axis current fluctuates from 0.1 to 0.5 A. The torque ripple is 233–257 N·m. Meanwhile, the $q$-axis current fluctuates at 7.07 ± 0.13 A, while the $d$-axis current fluctuates from 0.1 to −0.1 A with method 2. The torque ripple is about 237–243 N·m. The PFA increases as power output increases. The fluctuation of $dq$-axis current is more obvious in 1 kW. Meanwhile, the circularization of current vector trajectory on the $\alpha\beta$ plane performs well with method 2. Consequently, the experimental results correspond with the theory analyzed in Section II. The proposed control scheme can work well in the torque ripple reduction.

The experimental results of current zero crossing duration phenomenon are shown in Fig. 12. Fig. 12(a) and (b) presents the $a$-phase current and the corresponding voltage output by diode converter with method 1. The power output reference is set as 500 W and 1 kW, respectively. It can be seen that a current zero crossing duration exists as controlled with method 1. The durations lasts 3.8 and 8.2 ms for these two cases. As the power reference increases, the PFA increases and the zero crossing duration increase. It can be found that the zero crossing duration generates pulse disturbance in diode converter voltage output. With method 2, the zero crossing duration has been suppressed as shown in Fig. 12(c) and (d). It proves that the proposed method achieves a fast and unrepeated current zero crossing. Meanwhile, the pulse disturbance also decreases.

The dynamic performance of the semicontrolled open-winding PMSG system with the proposed method is demonstrated in Fig. 13. It can be seen that as the power step changes from 1 kW to 500 W as shown in Fig. 13(a), the system keeps stable and the current zero crossing duration keeps suppressed. The dynamic response time for the power changing is controlled

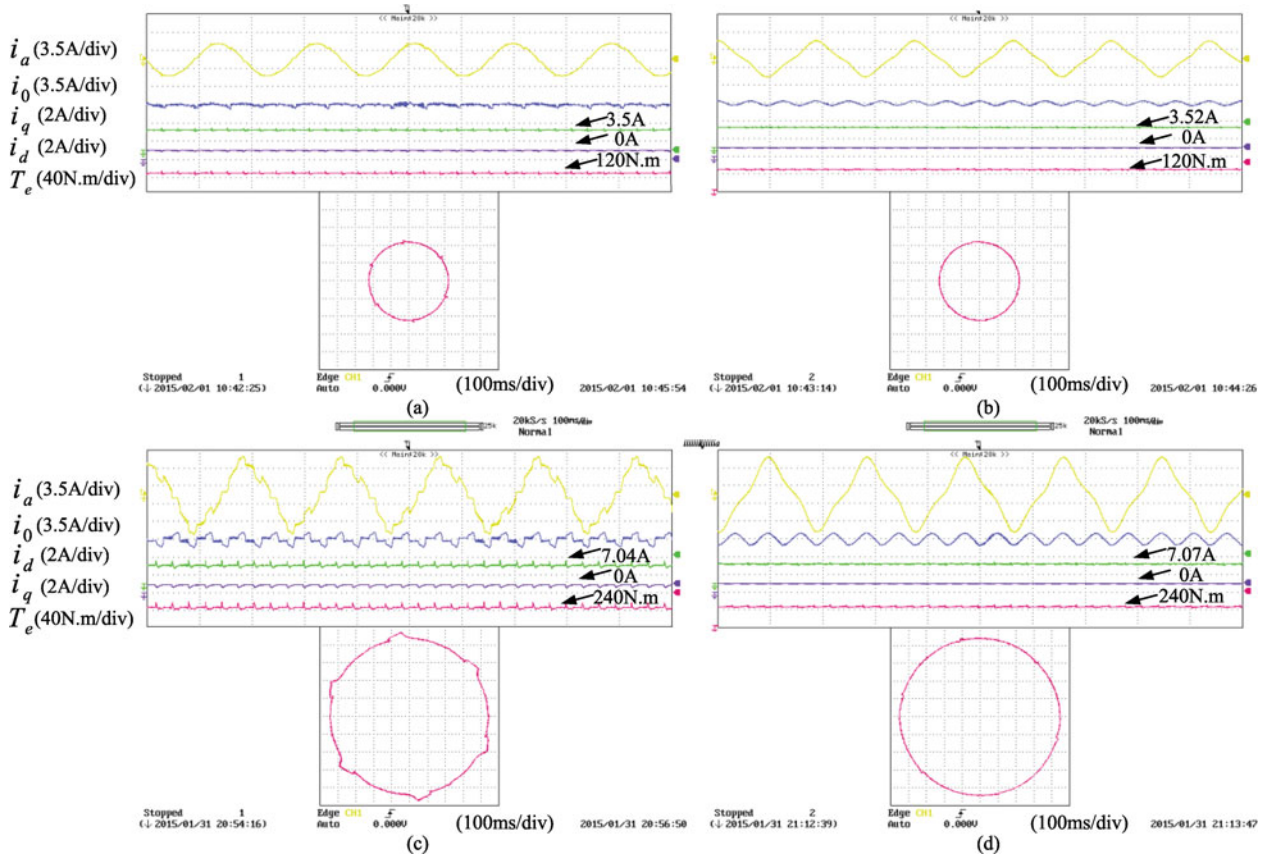


Fig. 11. Experimental results of the semicontrolled system. (a) Method 1 with 500-W power output. (b) Method 2 with 500-W power output. (c) Method 1 with 1-kW power output. (d) Method 2 with 1-kW power output.

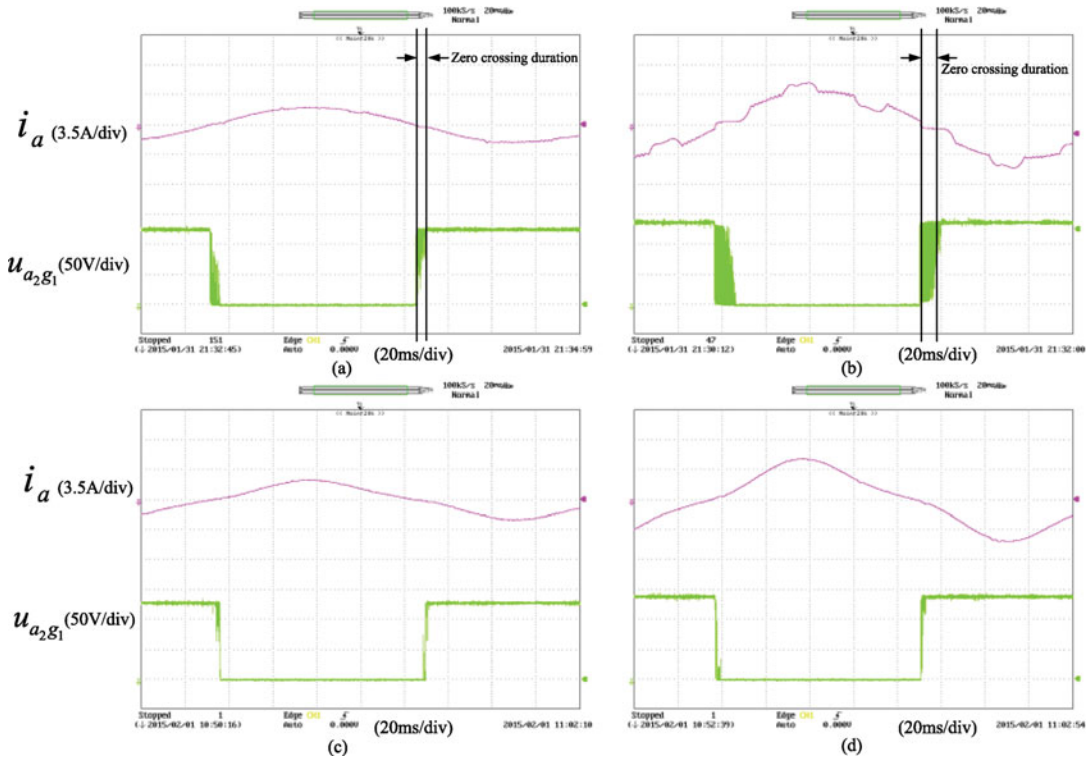


Fig. 12. Current zero crossing duration phenomenon and the voltage output by diode bridge. (a) Method 1 with 500-W power output. (b) Method 1 with 1-kW power output. (c) Method 2 with 500-W power output. (d) Method 2 with 1-kW power output.

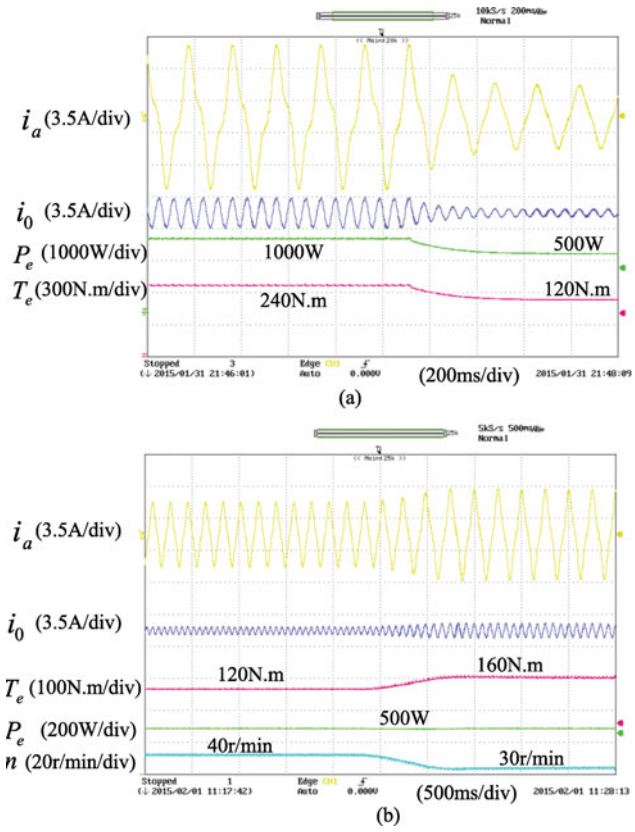


Fig. 13. Results of dynamic performance of the proposed third harmonic injection method. (a) Power change from 1 kW to 500 W. (b) Speed change from 40 to 30 r/min.

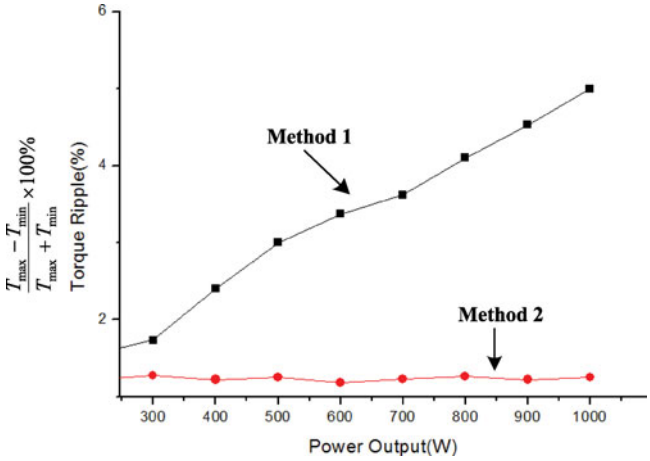


Fig. 14. Relationship between torque ripple and power output in the experimental open-winding PMSG system.

in 10 ms. The dynamic response with the proposed method on rotor speed changes from 40 to 30 r/min is demonstrated in Fig. 13(b). In this case, the power output is kept as constant 500 W. As the rotor speed changes, the resonant frequency will change. It can be seen that the PR regulator performs well in the dynamic process. The dynamic response time is controlled as 600 ms.

The relationship between torque ripple and power output based on the experimental PMSG is shown in Fig. 14. As the power output increase, the torque fluctuation increase with method 1. It reaches $\pm 5\%$ at the rated power output. However, with method 2, the torque fluctuation keeps at $\pm 1.25\%$. It can be concluded that the proposed method performs well in the torque ripple suppression.

## VIII. Conclusion

The current zero crossing phenomenon is an inherent drawback with nonzero PFA control method for the semicontrolled open-winding PMSG system. This paper gives a detailed analysis on the current vector trajectory in a 3-D perspective. Meanwhile, a third harmonic current injection method is adopted to reduce the zero crossing duration. With the third harmonic injection, the zero crossing point of the current is shifted to be synchronized with the voltage. A zero-sequence current regulator is proposed to modulate the desired third harmonic. Afterward, the performance of the third harmonic injection is demonstrated by the experimental results. From the comparison, it can be found that the torque ripple optimization performs well with the third harmonic injection. The dynamic responses also prove that the proposed PR controller is suitable for the zero-sequence current regulator.

## References

[1] M. A. Perez, S. Bernet, J. Rodriguez, S. Kouro, and R. Lizana, "Circuit topologies, modeling, control schemes, and applications of modular multilevel converters," *IEEE Trans. Power Electron.*, vol. 30, no. 1, pp. 4–17, Jan. 2015.

[2] J. Pereda and J. Dixon, "Cascaded multilevel converters: Optimal asymmetries and floating capacitor control," *IEEE Trans. Ind. Electron.*, vol. 60, no. 11, pp. 4784–4793, Nov. 2013.

[3] R. S. Kaarthik, K. Gopakumar, J. Mathew, and T. Undeland, "Medium-voltage drive for induction machine with multilevel dodecagonal voltage space vectors with symmetric triangles," *IEEE Trans. Ind. Electron.*, vol. 62, no. 1, pp. 79–87, Jan. 2015.

[4] S. Srinivas and J. Kalaiselvi, "Pulse width modulation schemes enabling single DC power source driven dual two-level voltage source inverter with single voltage source inverter switching," *IET Power Electron.*, vol. 7, no. 5, pp. 1181–1191, May 2014.

[5] N. A. Azeez, K. Gopakumar, J. Mathew, and C. Cecati, "A harmonic suppression scheme for open end winding split phase IM drive using capacitive filters for the full speed range," *IEEE Trans. Ind. Electron.*, vol. 61, no. 10, pp. 5213–5221, Oct. 2014.

[6] P. P. Rajeevan, K. Sivakumar, K. Gopakumar, C. Patel, and H. Abu-Rub, "A nine level inverter topology for medium voltage induction motor drive with open end stator winding," *IEEE Trans. Ind. Electron.*, vol. 60, no. 10, pp. 3627–3636, Sep. 2013.

[7] J. Kalaiselvi and S. Srinivas, "Bearing currents and shaft voltage reduction in dual-inverter-fed open-end winding induction motor with reduced CMV PWM methods," *IEEE Trans. Ind. Electron.*, vol. 62, no. 1, pp. 144–152, Jan. 2015.

[8] Y. Lee and J. Ha, "Hybrid modulation of dual inverter for open-end permanent magnet synchronous motor," *IEEE Trans. Power Electron.*, vol. 30, no. 6, pp. 3286–3299, Jun. 2015.

[9] R. Baranwal, K. Basu, and N. Mohan, "Carrier-based implementation of SVPWM for dual two-level VSI and dual matrix converter with zero common-mode voltage," *IEEE Trans. Power Electron.*, vol. 30, no. 3, pp. 1471–1487, Mar. 2015.

[10] J. Mathew, P. P. Rajeevan, K. Mathew, N. A. Azeez, and K. Gopakumar, "A multilevel inverter scheme with dodecagonal voltage space vectors based on flying capacitor topology for induction motor drives," *IEEE Trans. Power Electron.*, vol. 28, no. 1, pp. 516–525, Jan. 2013.

[11] K. Mathew, K. Gopakumar, J. Mathew, N. A. Azeez, A. Dey, and L. Umanand, "Medium voltage drive for induction motors using multilevel octadecagonal voltage space vectors," *IEEE Trans. Power Electron.*, vol. 30, no. 1, pp. 4–17, Jan. 2015.

[12] G. D. Marques and M. F. Iacchetti, "Stator frequency regulation in a field oriented controlled DFIG connected to a DC link," *IEEE Trans. Ind. Electron.*, vol. 61, no. 11, pp. 5930–5939, Nov. 2014.
[13] M. F. Iacchetti, G. D. Marques, and R. Perini, "A scheme for the power control in a DFIG connected to a DC bus via a diode rectifier," *IEEE Trans. Power Electron.*, vol. 30, no. 3, pp. 1286–1296, Mar. 2015.
[14] A. Venkataraman, A. I. Maswood, N. Sarangan, and O. H. P. Gabriel, "An efficient UPF rectifier for a stand-alone wind energy conversion system," *IEEE Trans. Ind. Appl.*, vol. 50, no. 2, pp. 1421–1431, Mar./Apr. 2014.
[15] J. Wang, D. Xu, B. Wu, and Z. Luo, "A low cost rectifier topology for variable speed high power PMSG wind turbines," *IEEE Trans. Power Electron.*, vol. 26, no. 8, pp. 2192–2200, Aug. 2011.
[16] D. S. Oliveria, M. M. Reis, C. E. A. Silva, L. H. S. C. Barreto, F. L. M. Antunes, and B. L. Soares, "A three phase high frequency semicontrolled rectifier for PM WECS," *IEEE Trans. Power Electron.*, vol. 25, no. 3, pp. 677–685, Mar. 2010.
[17] H. Nian and Y. Zhou, "Investigation on open winding PMSG system with the integration of full controlled and uncontrolled converter," *IEEE Trans. Ind. Appl.*, vol. 51, no. 1, pp. 429–439, Jan./Feb. 2015.
[18] Y. Wang, D. Panda, T. Lipo, and D. Pan, "Open-winding power conversion systems fed by half-controlled-converters," *IEEE Trans. Power Electron.*, vol. 28, no. 5, pp. 2427–2436, May 2013.
[19] H. Nian, Y. Zhou, and H. Zeng, "Zero sequence current suppression strategy for open winding PMSG fed by semicontrolled converter," *IEEE Trans. Power Electron.*, vol. 31, no. 1, pp. 711–720, Jan. 2016.
[20] F. Wu, B. Sun, K. Zhao, and L. Sun, "Analysis and Solution of current zero crossing distortion with unipolar hysteresis current control in grid connected inverter," *IEEE Trans. Ind. Electron.*, vol. 60, no. 10, pp. 412–420, Oct. 2013.
[21] R. Sharma and J. A. R. Ball, "Unipolar switched inverter low frequency harmonics caused by switching delay," *IET Power Electron.*, vol. 2, no. 5, pp. 508–516, Sep. 2009.
[22] J. Huang and H. Wei, "The current harmonics elimination control strategy for six-leg three-phase permanent magnet synchronous motor drives," *IEEE Trans. Power Electron.*, vol. 29, no. 6, pp. 3032–3040, Jun. 2014.
[23] P. Sandulescu, F. Meinguet, X. Kestelyn, E. Semail, and A. Bruyere, "Control strategies for open end winding drives operating in the flux weakening region," *IEEE Trans. Power Electron.*, vol. 29, no. 9, pp. 4829–4842, Sep. 2014.
[24] Y. Y. Xia, J. E. Fletcher, S. J. Finney, and K. H. Ahmed, "Torque ripple analysis and reduction for wind energy conversion systems using uncontrolled rectifier and boost converter," *IET Renew. Power Gener.*, vol. 5, no. 5, pp. 377–386, Feb. 2011.
[25] A. Venkataraman, A. I. Maswood, N. Sarangan, and O. H. P. Gabriel, "Improved switching frequency variation control of hysteresis controlled voltage source inverter-fed IM drives using current error space vector," *IET Power Electron.*, vol. 3, no. 2, pp. 219–231, Mar. 2014.
[26] R. Teodorescu, F. Blaabjerg, M. Liserre, and P. C. Loh, "Proportional-resonant controllers and filters for grid-connected voltage-source converters," *Proc. IEE Electr. Power Appl.*, vol. 153, no. 5, pp. 750–762, Sep. 2006.
[27] C. Xia, F. Zhou, Z. Wang, and X. He, "Equivalent switch circuit model and proportional resonant control for triple line voltage cascaded voltage source converter," *IEEE Trans. Power Electron.*, vol. 29, no. 9, pp. 4829–4842, Sep. 2014.
[28] H. Nian and Y. Song, "Optimized parameter design of proportional integral and resonant current regulator for doubly fed induction generator during grid voltage distortion," *IET Renew. Power Gener.*, vol. 8, no. 3, pp. 299–313, Apr. 2014.

**Heng Nian** (M'09–SM'14) received the B.Eng. and M.Eng. degrees from the Hefei University of Technology, Hefei, China, and the Ph.D. degree from Zhejiang University, Hangzhou, China, in 1999, 2002, and 2005, respectively, all in electrical engineering.

From 2005 to 2007, he was a Postdoctoral Researcher with the College of Electrical Engineering, Zhejiang University. In 2007, he was promoted as an Associate Professor. From 2013 to 2014, he was a Visiting Scholar with the Department of Electrical, Computer, and System Engineering, Rensselaer Polytechnic Institute, Troy, NY, USA. Since 2016, he has been a Full Professor at the College of Electrical Engineering, Zhejiang University. His current research interests include the optimal design and operation control for wind power generation system. He has published more than 20 IEEE/IET Transaction papers and holds more than 20 issued/pending patents.

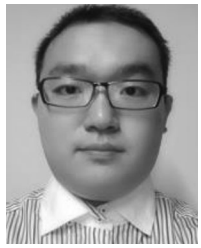

**Yijie Zhou** was born in Xiaogan, China, in 1990. He received the B.Sc. degree from the College of Electrical Engineering, Zhejiang University, Hangzhou, China, in 2011, where he is currently working toward the Ph.D. degree.

His current research interests include motor control with power electronics devices in renewable energy conversion, particularly the open-winding permanent magnet synchronous generator systems with the integration of multilevel converters.